

Design and manufacturing rules for maximizing the performance of polycrystalline piezoelectric bending actuators

Noah T Jafferis, Michael J Smith and Robert J Wood

School of Engineering and Applied Sciences, Harvard University, Cambridge, MA, USA
Wyss Institute for Biologically Inspired Engineering, Harvard University, Boston, MA, USA

E-mail: njafferis@seas.harvard.edu

Received 1 December 2014, revised 16 February 2015

Accepted for publication 25 March 2015

Published 11 May 2015



Abstract

Increasing the energy and power density of piezoelectric actuators is very important for any weight-sensitive application, and is especially crucial for enabling autonomy in micro/milli-scale robots and devices utilizing this technology. This is achieved by maximizing the mechanical flexural strength and electrical dielectric strength through the use of laser-induced melting or polishing, insulating edge coating, and crack-arresting features, combined with features for rigid ground attachments to maximize force output. Manufacturing techniques have also been developed to enable mass customization, in which sheets of material are pre-stacked to form a laminate from which nearly arbitrary planar actuator designs can be fabricated using only laser cutting. These techniques have led to a 70% increase in energy density and an increase in mean lifetime of at least 15× compared to prior manufacturing methods. In addition, measurements have revealed a doubling of the piezoelectric coefficient when operating at the high fields necessary to achieve maximal energy densities, along with an increase in the Young's modulus at the high compressive strains encountered—these two effects help to explain the higher performance of our actuators as compared to that predicted by linear models.

 Online supplementary data available from stacks.iop.org/sms/24/065023/mmedia

Keywords: piezoelectric, actuators, fracture strength, high field/high strain effects, energy density optimization

(Some figures may appear in colour only in the online journal)

1. Introduction

1.1. Importance of improving energy density, lifetime, and manufacturability

We report on efforts related to material processing, optimization, and testing of PZT-5H used to manufacture actuators for microrobots, with the goal of improved robustness and transducer efficiency. Maximizing power density and fracture strength is especially crucial for small robots [1–5] and other devices (such as mechanical grippers [6], micro-valves [7],

adaptive optics [8], knitting machines [9], braille displays [10], and many more) that rely on oscillating power delivery, as weight can be a limiting factor. Besides being readily available, PZT-5H is chosen for its combination of high piezoelectric coefficients and modulus, while maintaining relatively high fracture strength (compared with single-crystal PZT, for example). Additionally, the processing considerations described in this work are likely to be applicable for increasing fracture strength in other polycrystalline ceramics as well. While bulk PZT can produce very high forces, its displacement is typically too low (sub-micron) for powering

Table 1. Comparison of roughnesses and failure strengths for several PZT machining methods.

	Anton <i>et al</i> [11]	Misri <i>et al</i> [12]	Annoni <i>et al</i> [13]	Our results
σ_{\max}	115 MPa			145–160 MPa
ϵ_{\max}	0.26%			0.29–0.32%
R	8 μm^a	<1 μm^b	3.5 μm^b	0.1–0.7 μm^c

^a Flaw size.^b R_a .^c R_q .

micrometer to centimeter scale mechanisms, even with the use of mechanical transmissions. Hence, the standard bimorph actuator configuration is utilized as a strain amplification mechanism, in which two plates of PZT are bonded together so that the actuator bends as the voltages on each plate are varied. This bending results in relatively high tensile surface strain on the PZT, which can induce fractures leading to actuator failure. Typically, when a brittle material is cyclically strained, the closer it gets to the instantaneous failure strain during this cycling, the fewer cycles it can withstand. Hence, increasing the failure strain not only allows greater instantaneous bending before fracture, it is also expected to increase lifetime when operated at the same strain levels.

Before moving on to our approach for improving these aspects of actuator performance, we look briefly at the current state-of-the-art for manufacturing PZT bimorph actuators:

1.2. Current state-of-the-art

A variety of methods for machining PZT (since we are focusing on bulk polycrystalline materials, rather than sol-gel deposition, for example, the PZT plates must be cut in order to produce the desired shape) have been explored, including diamond saws [11], powder blasting [12], water jet [13], and lasers [14, 15] (also, see [12] for an overview of some of these methods). Table 1 compares failure strengths/roughnesses resulting from some of these methods, as well as from the process described in this work. Compared to the other available methods, several advantages of laser-cutting are small feature size and cut width, the ability to cut complex patterns, and relatively clean cuts, but heating can be problematic if not properly controlled. In addition to machining the bulk PZT, it must also be bonded together and assembled to produce bimorph actuators. One approach is to use an inactive central layer, such as carbon fiber composite (CF), that bonds the PZT together and provides electrical contact, as in [16]. Other methods include interdigitated electrodes on a single PZT plate [17], which can harness the typically higher d_{33} coefficient but the electric field doesn't penetrate through the entire material thickness.

2. Maximizing energy density and lifetime

In order to maximize the energy density and lifetime of piezoelectric actuators, we proceed along two routes: increasing the

fracture strength of the bulk PZT plates (covered in this section) and improved manufacturing techniques that both increase the available force output and distribute strain more uniformly along the length of the actuator (covered in section 3).

2.1. Flexural strength (mechanical)—bulk PZT

2.1.1. Edge treatment—laser or polishing reduces local surface roughness. To develop a method for improving the flexural strength of PZT we hypothesize that crack formation initiates at grain boundaries on the cut edges of the samples (i.e. intergranular fracture—this is the more common mode of fracture for soft PZT materials like PZT-5H [18]). If this is the case, then reducing the edges' surface roughness at the scale of the grain size should increase flexural strength. We test this through two methods for surface roughness reduction—mechanical polishing and laser-induced melting.

We use a diode-pulsed solid-state laser (Photonics Industries DC150H-355, a Nd:YVO4 laser with 355 nm wavelength) to cut sheets of material through ablation—a pulsed laser is used to achieve higher instantaneous power density and the shorter time of exposure means that less heating of the surrounding material occurs, resulting in a 'cold' ablation process. However, as we shall see shortly, the evidence indicates that localized melting does occur, at least for the PZT. The laser has a maximum average power output of 0.63 W (measured at the workpiece) when operated at 20 kHz. At this frequency, the pulse duration is 16 ns, resulting in an instantaneous power of 2 kW during each 32 μJ pulse. The beam is also highly focused—its spot size of about 10 μm in diameter leads to maximum average power densities of 8 GW m^{-2} and maximum instantaneous power densities of 25 TW m^{-2} . As a comparison, our energy density per pulse is 40 J cm^{-2} (and down to 15 J cm^{-2} for lower power cuts), while [14] used 13–38 J cm^{-2} , and [15] went up to 70 J cm^{-2} . Throughout this paper, we will refer to the average power used for various laser treatments, but keep in mind that it is the power density that is crucial for achieving the desired effects.

To test the effect of mechanical polishing, PZT samples are first laser scored and cleaved (i.e. the material is placed between two glass slides, with the laser-score lined up with the edge of slides, and then pressed carefully until it cleaves at the score line)—this provides a much straighter edge than samples that are only cleaved. The PZT is then placed into a fixture and the sample sides parallel to the longitudinal axes are polished using 1200/inch grit polishing paper until a smooth curved edge is achieved. This reduces surface irregularities and produces a full radius in place of the sharp edges (which is expected to be an additional benefit for fracture strength) per ASTM Testing Standard C1161-02C (2008).

To measure the effect of the laser or polishing on edge roughness, we prepared samples cut at various laser powers part of the way through the sample, followed by cleaving. This allows a comparison to be made between the portion of each sample that is cleaved and the portion that is laser-treated. Using a confocal laser microscope, we take images of the exposed edges of the PZT and measure the roughness for

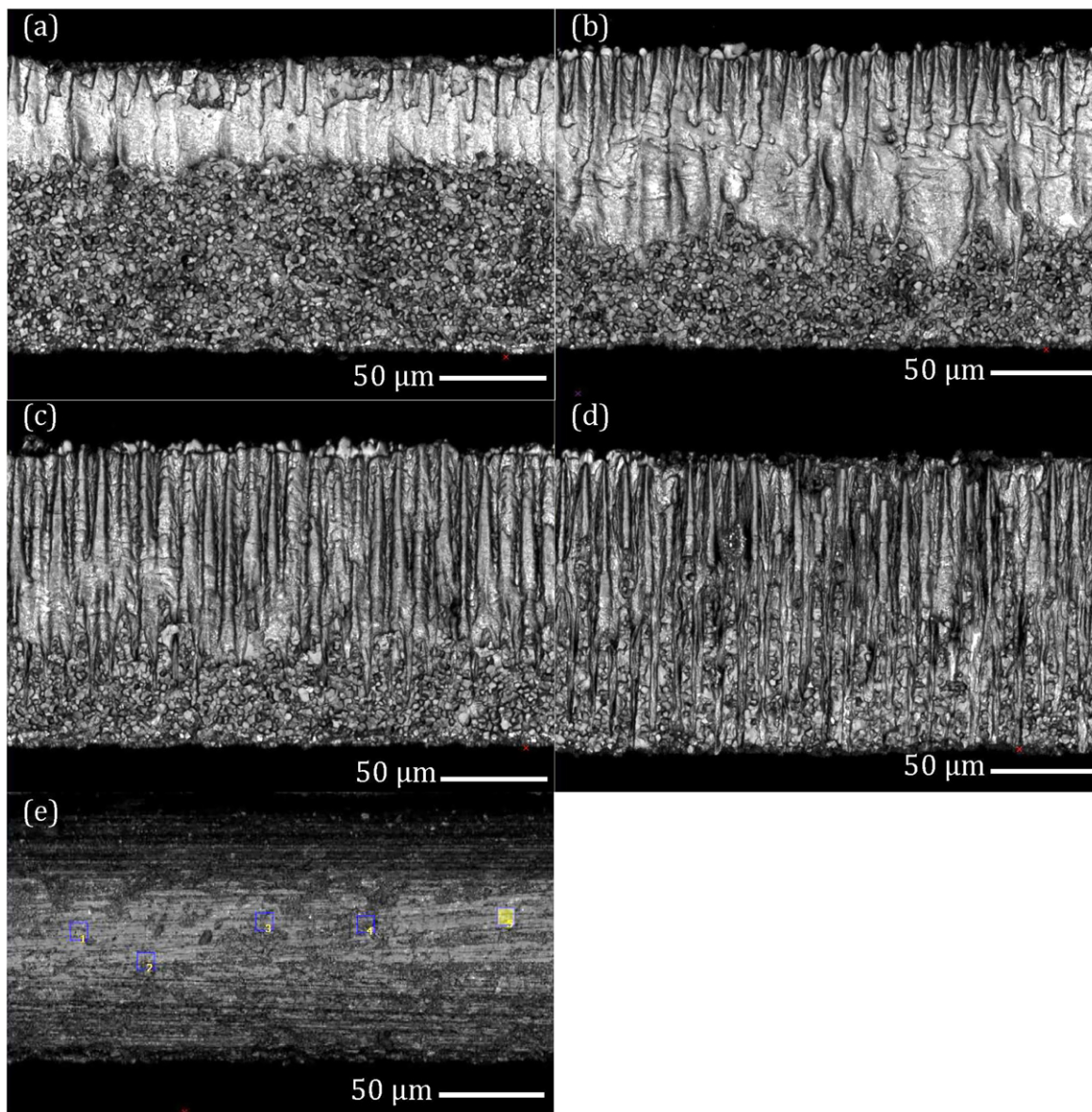


Figure 1. (a) Cut about 30% through using 0.63 W laser power; the remainder is cleaved. (b) Cut about 60% through using 0.58 W laser power; the remainder is cleaved. (c) Cut about 70% through using 0.40 W laser power; the remainder is cleaved. (d) Cut 50–80% through using 0.23 W laser power; the remainder is cleaved. (e) Sample laser scored and cleaved, followed by polishing (the boxes labeled 1–5 are regions from which roughness measurements were taken). All images are intensity maps taken with a confocal microscope using the same lighting (for (a)–(d)).

each sample. The resulting images are shown in figure 1, with the following sample treatments: (a)–(d) are scored with the laser to about half-way through the material (30–70%), at powers of 0.63, 0.58, 0.40, and 0.23 W, respectively, and (e) is cleaved and then polished. At a large scale (10s of microns), parallel ridges and troughs can be seen in the laser-cut samples—this is a result of the pulsed nature of the laser beam (combined with the lateral speed of travel). However, on the scale of the grain size (a few microns), the roughness is seen to decrease by a factor of 2–3 with increasing laser power—a plot of this roughness versus laser power is shown in figure 2; the roughnesses for the cleaved and polished samples are also indicated, showing that mechanical polishing also reduces the roughness substantially (to slightly lower roughness than that achieved with the full-power laser

treatment). Interestingly, the laser power that is required to cause a significant reduction in roughness increases as the size-scale over which the roughness is measured increases—from 0.4–0.6 W at the 30 μm scale, to 0.2–0.4 W at 8 μm , to 0–0.2 W at 3 μm . We postulate that this is due to the following phenomenon: as the size-scale over which the roughness is measured increases, the measurement effectively probes greater depths away from the idealized location of the cut (i.e. into the page for the images shown in figure 1). Since the depth to which the material is melted is expected to increase with increasing laser power, this would result in the observed behavior. This effect is useful, because it allows us to estimate the relevant size-scale for the material properties that we are trying to improve (e.g. flexural strength)—that is, after determining the power that is needed to significantly

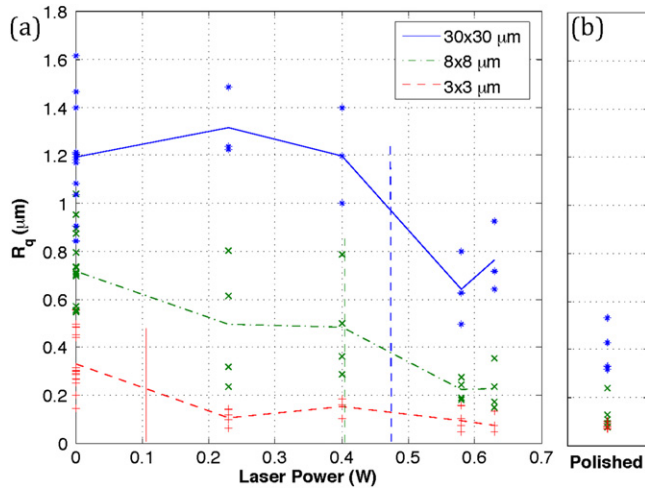


Figure 2. (a) Roughness versus laser power for several size-scales. The vertical lines indicate ‘transitions’ in the roughness—i.e. where the roughness has dropped about half-way from its ‘low-power’ to ‘high-power’ value. (b) Roughness after polishing. Measurements were taken in 4–6 randomly chosen regions from each of the laser-scored/cleaved and polished samples shown in figure 1.

effect the property in question, figure 2 can identify the size-scale which results in significant roughness reduction/surface melting at that power. Further, we note that after such melting and resolidifying, the affected material is no longer expected to be stoichiometric PZT due to incongruent melting [19]. To confirm this, we take several EDS measurements to compare cleaved and laser-treated areas. The results, shown in figure 3, indicate that the new material has an enhanced percentage of Zr and Ti, which is likely due to preferential vaporization of PbO [19]. A trace of Ni is also detected, but in both the cleaved and laser-treated areas—this is thus likely due to contamination from the Ni coating on the electrodes of the initial PZT samples. The EDS measurements probe to a depth of a few microns, which may be similar to the thickness of the melted layer. Hence, while these measurements clearly show a significant composition change, they may not provide exact values.

Now that we have methods for reducing the edge roughness of the PZT at the scale expected to be relevant, we determine the effect of this roughness reduction on flexural strength through the use of four-point bend tests (see a diagram of this setup in figure 4). An Instron material testing machine is used to bend beams of PZT 25 mm long, 2 mm wide (b), and 140 μm thick (d)—the width is chosen to be equal to the average width of our standard actuators, while the length is made just long enough to be easily mounted in the Instron. The maximum strain (ϵ) and stress (σ) at the beam’s surface are calculated from the applied deflection (δ) and measured force (F) using the standard equations:

$$\epsilon = \delta \times \frac{6d}{(L_o - L_i)(L_o - 2L_i)} \quad (1)$$

$$\sigma = F \times 1.5 \frac{L_o - L_i}{bd^2} \quad (2)$$

where L_o and L_i are support span and load span, respectively (as defined in figure 4). In these bending tests, only one side of the beam experiences tension (which is expected to trigger fracturing), while the other side experiences compression. Similarly, in the bimorph actuators that are the intended application of these methods, the outer surface experiences much greater tension than the inner surface (which is close to the neutral axis). Hence, we hypothesize that the fracture strength may only need improvement on the side of the sample which experiences tension. To test this effect, PZT beams are fabricated by first scoring to various depths with the laser (at 0.63 W power), followed by cleaving to complete the cut. The flexural strength is then measured both for samples with the laser-cut side in tension, and for samples with the cleaved side in tension. As can be seen in figure 5(a), the failure strength is 10–25% greater when the laser-cut side is in tension (up to 145–160 MPa and 0.29–0.31% strain, as compared to 115–130 MPa and 0.24–0.25% strain when the cleaved side is in tension), with the improvement increasing with increasing cut depth up to 65–80% cut depth. Once the laser has completely cut through the sample, the flexural strength is nearly identical regardless of which side is in tension. In addition, a comparison with others’ reported flexural strength data [11] shows that our results with the laser-cut side in tension are 25–40% higher in failure stress (145–160 MPa versus 116 MPa) and 10–20% higher in failure strain (0.29–0.31% versus 0.26%) (see figure 5(a)). In figure 5(b), we show the dependence of flexural strength on laser power—0.23 W of power has essentially no effect on the flexural strength, but by 0.4 W, a significant increase has occurred. Further increase of laser power up to 0.63 W provides only slight improvement. Comparing this transition power of about 0.3 W to the roughness measurements, we see that this corresponds to a size scale of 3–8 μm —since the material grain size is about 4 μm , this supports the notion that the improvement in flexural strength is a result of the removal of grain boundaries through surface melting. From these measurements, cutting 65–100% of the way through the PZT using 0.63 W power gives the best results in terms of flexural strength, but we will see in section 2.2 that dielectric strength must be taken into account to achieve fully optimized performance. Additionally, the flexural strength was measured for polished samples, and found to be about 10% greater than unpolished ones (figure 5(c)).

2.1.2. Crack-arresting features. While the previous section showed that reducing edge roughness increases the maximum strain that the PZT can withstand before cracking, we now present a method to slow crack propagation once it has begun, resulting in further increases in ultimate flexural strength: slots are laser-cut on the broad face of rectangular PZT test samples, parallel to the material longitudinal axis (figure 6(a)), to investigate crack-arresting properties. Due to random variation in stress riser location, crack propagation doesn’t proceed directly across the sample when the slots are scored at least 80% of the way through the material. Rather, the crack is displaced laterally as it crosses each slot, by as much as several mm

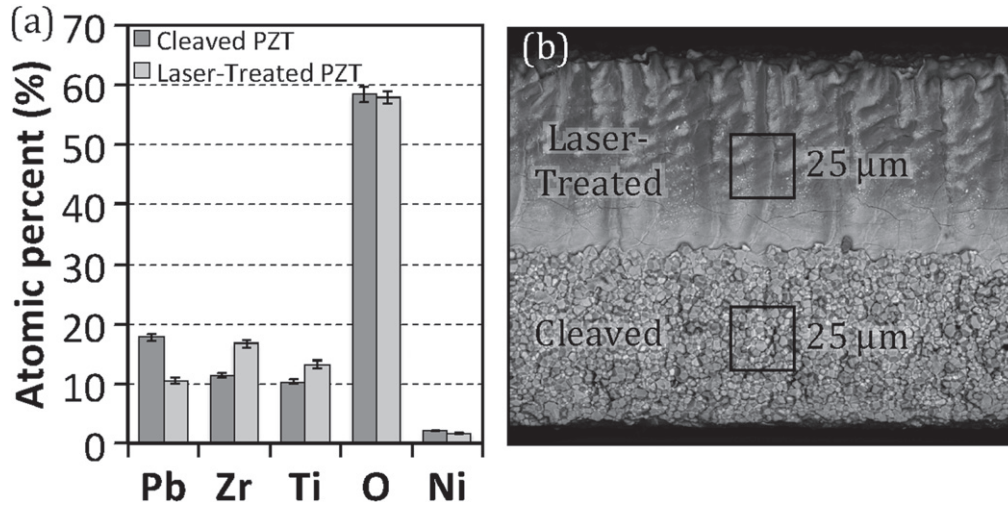


Figure 3. (a) EDS measurements (taken from two laser-scored and cleaved PZT samples) comparing the relative percentages of each element in laser-treated PZT (four measurements) to those in cleaved PZT (four measurements). The error bars show one standard deviation. (b) An SEM image showing representative cleaved and laser-treated areas.

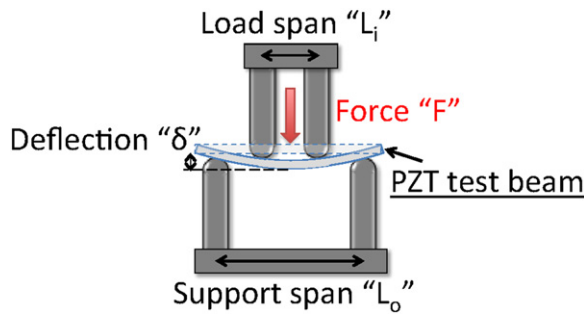


Figure 4. Four-point bend tests on PZT beams.

(figure 6(a)). The idea here is that separating the beam into a number of parallel narrower beams can effectively change the mode of failure from a single abrupt catastrophic failure to a series of smaller failures. As seen in figure 6(b), the initial failure (cracking to the first slot) strain increases by 8%. The stress at initial failure decreases by 4% (after adjusting for the smaller width of the slotted samples—each of the 3 slots is 20–30 μm wide, leading to a width reduction of 3–5%). The strain when the crack has propagated to the third slot is 14% greater than no-slot samples, while the adjusted stress (i.e. once some regions of the sample have cracked, its width is reduced) is approximately unchanged. This increase in failure strain could be useful for actuators because in practice the PZT layers are adhered to a central carbon fiber layer, and the metal coating on the PZT conducts around the crack. If the slots are scored less than 65% of the way through, no significant effect is observed, indicating that crack propagation is not confined to the surface.

2.2. Dielectric strength (electrical)—bulk PZT

2.2.1. Effect of laser treatment and polishing on dielectric strength. Based on the results of section 2.1.1, cutting completely through the PZT is an attractive option—this would also allow for faster manufacturing (i.e. laminating

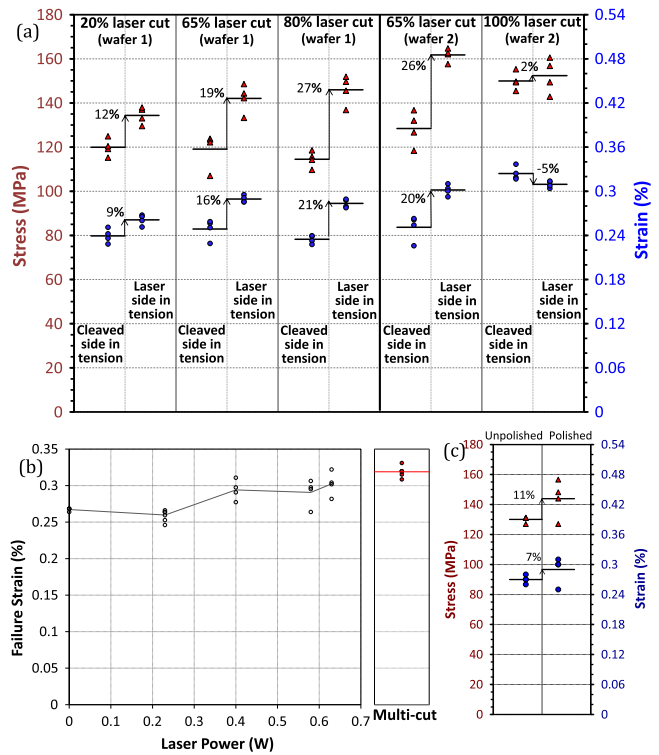


Figure 5. (a) Effect of laser-score orientation and score depth (four-point bend test). All cuts were performed using max laser power (0.63 W). The failure stress (triangle markers) and failure strain (circle markers) are shown for various laser-cut depths, and both with the laser-cut side in tension and with the cleaved side in tension. Four samples were tested for each condition. Also shown are dashed lines representing the values obtained by Anton *et al* in [11]. (b) Effect of laser power on failure strength. All samples are cut completely through with the laser. The data at ‘zero laser power’ is from a laser-cut and cleaved sample with the cleaved side in tension. Also shown are the results from the ‘multi-cut’ process (a low-power through-cut followed by a high-power edge treatment) described in section 2.3. (c) Effect of polishing on failure strength. Measurements were taken for 3–5 samples in each testing condition for plots (a)–(c); all results are plotted.

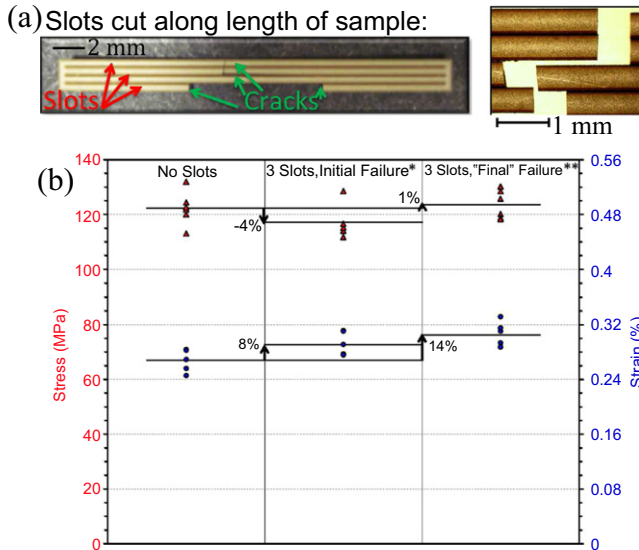


Figure 6. (a) Photos showing slots cut along the length of the PZT sample, and cracks (after four-point bend testing) whose propagation has been stopped or shifted by the presence of the slots. (b) Failure strength (triangles = stress; circles = strain) for samples with slots compared to those without slots. For all samples, the laser-cut side is in tension, the outside is cut about 65% through, and the slots are cut 100% through. *The stress is adjusted to account for reduction in sample width due to the slots. **The stress is adjusted to account for the actual sample width before the 'final' crack (i.e. once one or more of the regions between slots have cracked, the sample is narrower). Note: for several of these samples, the test stopped even though one quarter-width of the sample was still intact. Measurements were taken for 5–6 samples in each testing condition; all results are plotted.

sheets of PZT and CF first, and then cutting out completed actuators—see section 3) and could reduce variability by providing a more automated/less manual process. However, high-voltage tests reveal that cutting at maximum laser power (0.63 W) reduces the dielectric breakdown strength to only $1 \text{ V } \mu\text{m}^{-1}$. These tests are performed after coating the samples with cyanoacrylate (CA) glue or parylene to enable testing at fields higher than the dielectric strength of air. In figure 7, it can be seen that the PZT's dielectric strength drops rapidly with increasing laser power—even at only 0.4 W, it is already down to $2.7\text{--}3 \text{ V } \mu\text{m}^{-1}$. This is much less than the $> 6.4 \text{ V } \mu\text{m}^{-1}$ achieved for cleaved PZT (this was the limit of the test setup, and is thus a lower bound on the dielectric strength), and too close to the $2.2 \text{ V } \mu\text{m}^{-1}$ that our PZT actuators have previously been driven to. Laser-scored (about 50% through) and cleaved samples achieved $5 \text{ V } \mu\text{m}^{-1}$. Hence, if we are to completely cut through the PZT with a laser, it must be done at powers below about 0.3 W. This power is sufficiently low that the flexural strength would no longer be expected to improve much (see section 2.1)—essentially, it appears likely that the same physical process (i.e. surface melting) is the cause of both the increased flexural strength (i.e. due to the elimination of grain boundaries) and the decreased dielectric strength (likely due to the change in chemical composition—see section 2.1.1), leading to an intrinsic trade-off between these two properties. However, because the failure strain only needs to be

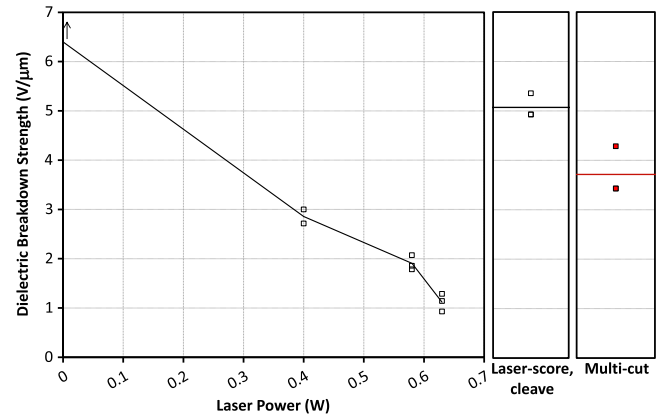


Figure 7. Dielectric breakdown strength of 2 mm by ~ 10 mm PZT samples cut completely through using various laser powers. Also shown is data for samples scored about 50% deep with 0.63 W laser power, followed by cleaving, as well as for samples cut using the 'multi-cut' process described in section 2.3. The solid lines represent the mean values of the various data. The arrow at zero laser power indicates that the dielectric strength shown is a lower bound—all three samples reached the limit of the test setup. Measurements were taken for three samples in each testing condition; all results are plotted.

improved near the surface experiencing the most strain, rather than through the entire material thickness, this trade-off can be at least partially avoided. Thus, laser-scoring and cleaving is still an option, but for the reasons discussed at the beginning of this section, we would like a way to use only the laser. A method to achieve this by combining low-power and high-power cuts is presented in section 2.3. In addition, uncoated polished samples were also tested to determine whether polishing effects dielectric strength in the same way as laser-induced melting does. Note that polishing removes some of the metal coating on the PZT, resulting in an increased distance (about 1.5 times farther for a full radius) between the electrodes—taking this into account, the breakdown fields achieved for these samples were $3 \text{ V } \mu\text{m}^{-1}$ (which is less than the air-breakdown of around $4 \text{ V } \mu\text{m}^{-1}$ measured for uncoated cleaved-only samples as noted in section 2.2.2 below). This suggests that polishing does not reduce the breakdown field by as much as the full-power laser (which resulted in $1 \text{ V } \mu\text{m}^{-1}$); but is perhaps similar to using the laser at 0.4 W.

2.2.2. Coatings to prevent electrical breakdown. To take full advantage of the increased flexural strength, the dielectric breakdown strength needs to be increased beyond that of air. To achieve this, the edges of some PZT samples (where shorts between the top and bottom electrodes would occur) are coated with CA glue, while others are coated with parylene ($3\text{--}4 \mu\text{m}$)—as can be seen in figure 8(a), this allows mean fields of $5.2 \text{ V } \mu\text{m}^{-1}$ for the CA glue case, and at least $6.4 \text{ V } \mu\text{m}^{-1}$ (the test limit) for the parylene case, to be applied before breakdown. In comparison, uncoated samples typically shorted at $\sim 3.9 \text{ V } \mu\text{m}^{-1}$. These samples were all cleaved

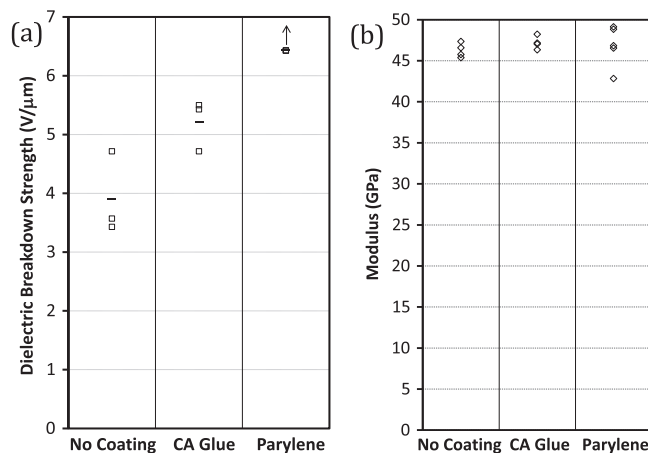


Figure 8. (a) Effect of coatings on electric breakdown. The arrow for the parylene-coated samples indicates that the dielectric strength shown is a lower bound—all three samples reached the limit of the test setup. (b) Effect of coatings on material stiffness. Measurements were taken for 3–5 samples in each testing condition; all results are plotted.

manually in order to test only the intrinsic PZT and/or coating dielectric strength.

In order for edge coating to be a useful means of improving dielectric strength, it must have minimal effect on the material stiffness—in figure 8(b), we show a comparison of modulus values (calculated from four-point bend tests) for uncoated, CA glue coated, and parylene coated samples. The results show that the CA glue increases the modulus by 2%, whereas the parylene increases it by 1%. Both of these measurements are within sample variation, but in any case, the parylene does better at increasing dielectric strength, and may improve the failure strain slightly (about 5%), so we will use only parylene for the remainder of the experiments involving coatings described in this paper.

2.3. Optimal sample preparation

We now present a solution to the dilemma of high laser power increasing flexural strength but decreasing dielectric strength. Since we have already demonstrated that most of the flexural strength improvement is achieved with cuts 65–100% of the way through the sample (since only one side of the PZT experiences tension, both in these material tests, and in the final actuator), we propose the following: first cutting all of the way through the PZT at sufficiently low power to avoid dielectric breakdown, then using a high-power laser to melt just the top part of the cut surface (see diagram and microscope image in figure 9). This allows us to take maximal advantage of the laser-induced melting by restricting it to only those regions where it is most beneficial for fracture strength. To do this requires very precise alignment with the existing cut edges, otherwise the depth to which the high-power laser effects the PZT will be variable and could cause local shorting. If the side-wall from the low-power cut is close to vertical (which is the case for our samples, as seen in figure 9), the required precision can be approximated by the

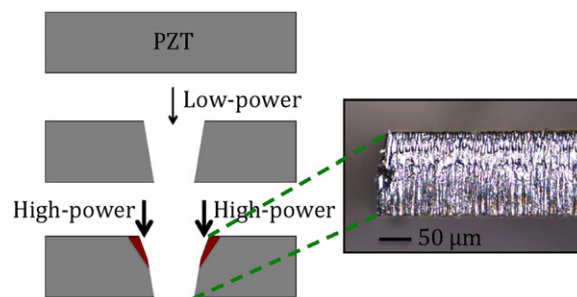


Figure 9. Cross-section diagram and photo depicting the multi-cut process—a low-power through-cut followed by offset high-power cuts to induce melting only near one side of the PZT.

lateral shift that would result in some specified change in the beam intensity at the edge of initial through-cut. For example, based on the plot of dielectric breakdown versus laser power (figure 7), even a change of 0.05 W would reduce the dielectric strength by about $0.5 \text{ V } \mu\text{m}^{-1}$ (note: the desired beam position is such that it is as close as possible to the existing cut edge in order to produce a sloping edge from the high-power cut, rather than a step; but not so close as to expose the entire low-power side-wall to the high-power laser). Assuming a Gaussian beam intensity profile, and noting that our high-power cut is at 0.63 W , while the maximum acceptable level for the low-power cut is 0.23 W , we obtain a desired precision of about 10% of the spot size (which gives $1 \text{ } \mu\text{m}$ for our case). The optimal offset of the high-power cut also depends on the width and steepness of the initial cut, so any changes in these would necessitate a change in the offset. For our cuts, offsetting the high-power edge treatment cut by $10 \text{ } \mu\text{m}$ from the low-power through-cut was found to melt the PZT's exposed edge about 50% of the way down from the surface (figure 9). Figures 5(b) and 7 show the performance results of samples prepared in the above manner, using 0.23 W for the low-power through-cut and 0.63 W for the high-power edge treatment—the mean dielectric strength (figure 7) is $3.7 \text{ V } \mu\text{m}^{-1}$, and the mean failure strain (figure 5(b)) is 0.32% (slightly higher than the 0.3% measured for laser-scored and cleaved samples). While the dielectric strength is lower than that achieved by laser-scoring and cleaving (since even the 0.23 W cut reduces the dielectric strength), it is still higher than the voltages at which we typically operate, and the increase in failure strain makes this a desirable compromise for our applications.

2.4. Other considerations

Before we move on to actuator fabrication, there are a few other considerations to keep in mind. The first is that all of the flexural strength tests described so far were performed with no electric field applied (i.e. open-circuit). Since the actuators that will be made from this material require high fields to operate, it is important to check whether this has any effect on the flexural strength. Figure 10(a) shows that it does have quite a strong effect—the mean failure strain decreases rapidly from 0.30% at $0 \text{ V } \mu\text{m}^{-1}$ to 0.21% at $1.5 \text{ V } \mu\text{m}^{-1}$,

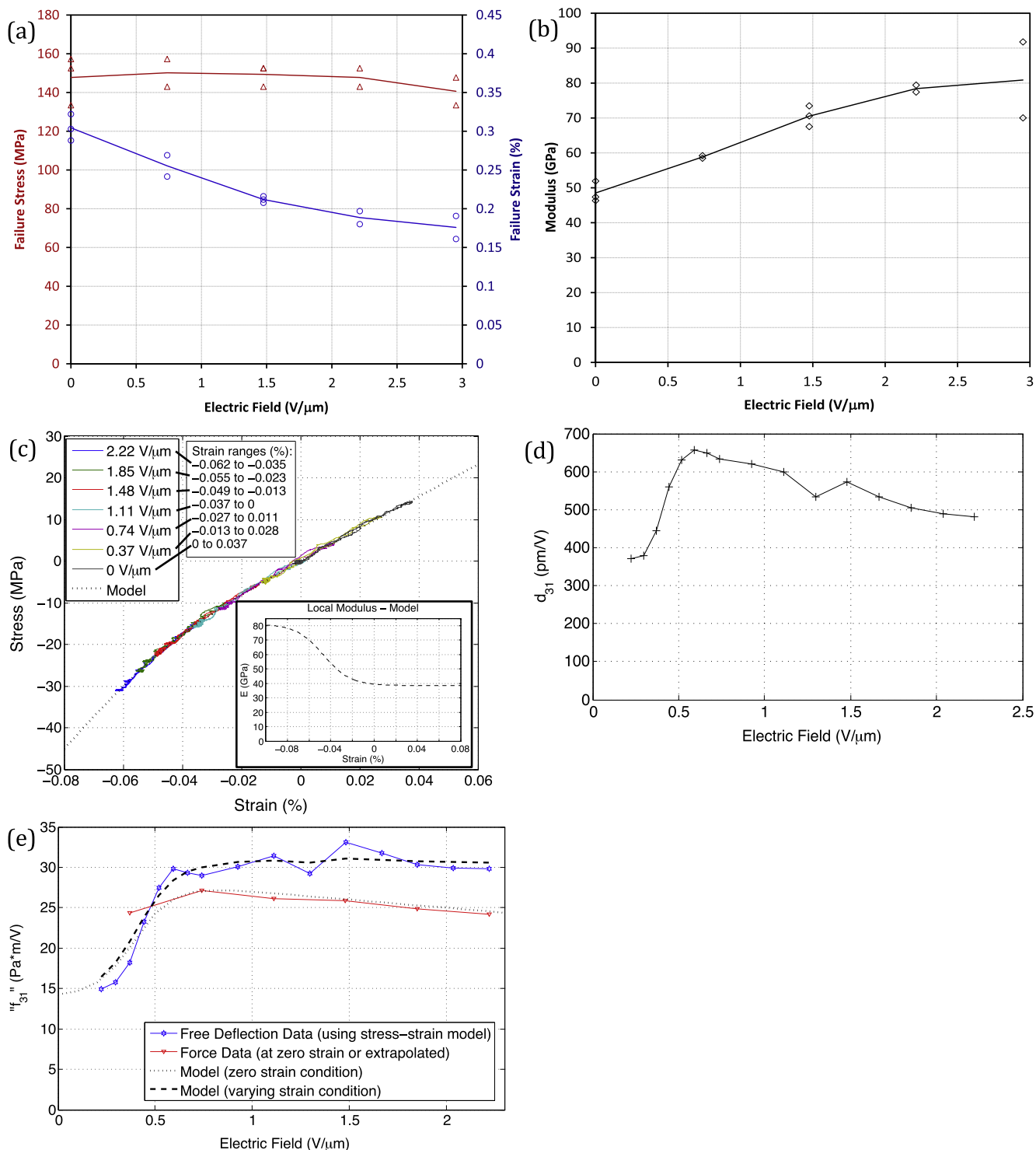


Figure 10. (a) PZT failure strength (triangles = stress; circles = strain) and (b) Young’s modulus, plotted as a function of electric field. Measurements were taken for 2–3 samples in each testing condition in parts (a) and (b); all results are plotted. (c) Modulus measurements using pulling setup. The inset shows the tangent modulus resulting from the model fit to the stress–strain data. (d) Directly measured d_{31} as a function of applied electric field. (e) f_{31} for two scenarios—free contraction (using d_{31} and stress–strain measurements), and blocked force (from stress–strain measurements at zero strain). A single model that incorporates the variation of f_{31} with field and strain is plotted for the two scenarios.

then a slower decrease to 0.18% at $3 \text{ V } \mu\text{m}^{-1}$ (400 V for our 135–140 μm thick samples). Note that the failure stress appears to be mostly independent of field (figure 10(a))—this is due to an increase in the modulus (figure 10(b)). It should

be pointed out here that in these experiments, the beam is free to contract when the electric field is turned on (before the four-point bend test begins)—that means that this experiment does not distinguish between electric field and compressive

strain as the physical cause of the decrease in failure strain and increase in modulus. In fact, we will show shortly that the modulus effect, at least, is actually due to the compressive strain rather than the electric field.

In order to determine whether the modulus is actually dependent on electric field, strain, or some combination, we need to be able to measure the stress–strain relation for various applied electric fields. Toward this end, we fabricate a 4 cm long beam of PZT and affix a reflective marker near each end so that the PZT's contraction can be detected using fiber optic sensors (Philtex D21). Then, one end is glued to a fixed stand while the other end is glued to a force sensor (Nano17) mounted on a calibrated translation stage. Adjusting the micrometer stretches the PZT beam, but the fiber optic sensors are still needed to accurately and precisely measure the strain in the beam as the glue used to affix each end of the beam stretches slightly as well. This stretching of the bond is actually beneficially for this measurement, as it allows us to probe negative (i.e. compressive) strains as well as extensive ones. Finally, electrical contact is made to each side of the PZT so that an electric field can be applied during the tests. For each voltage applied, the beam is stretched and returned to its starting length, resulting in a stress–strain plot that probes different but overlapping strains for each voltage. The measured stress during each test is the sum of the stress induced by the applied electric field and the stress produced by the external force—since it is this latter stress that we are interested in, we would like to subtract the contribution from the applied field. This contribution is simply the stress for which the strain is zero—for electric fields of $1.11 \text{ V } \mu\text{m}^{-1}$ and below, the sample was pulled sufficiently to pass through the zero-strain point, so this value is clear. For each stress–strain measurement obtained at electric fields higher than $1.11 \text{ V } \mu\text{m}^{-1}$, we proceed as follows: first, find the strain closest to zero for that field. Second, shift the data so that the stress at that strain matches the stress for all of the lower fields that probed that strain. The resulting plot is shown in figure 10(c). As can be seen, the plots produced for each applied field overlap nearly perfectly for strains that were present for multiple applied fields. This is the case even for the higher fields that do not pass through zero strain—even though those curves were lined up manually at one strain, their slopes (i.e. the tangent modulus) match well with those of other fields. This demonstrates that the primary contributor to the variation in modulus is actually the strain, and not the electric field. We also plot in figure 10(c) a simple fit to the data in which the modulus changes from one constant value at high extensive strain to a different constant value at high compressive strain (the inset shows this tangent modulus as a function of strain). The expression used for this fit is:

$$\sigma = \epsilon \cdot E_{\min} - \frac{E_{\max} - E_{\min}}{a} \left(\ln(1 + e^{a(\epsilon_0 - \epsilon)}) - \ln(1 + e^{a\epsilon_0}) \right), \quad (3)$$

$$E = \frac{\partial \sigma}{\partial \epsilon} = E_{\min} + (E_{\max} - E_{\min}) \frac{e^{a(\epsilon_0 - \epsilon)}}{1 + e^{a(\epsilon_0 - \epsilon)}}, \quad (4)$$

where $E_{\min} = 38.5 \text{ GPa}$, $E_{\max} = 81 \text{ GPa}$, $\epsilon_0 = -0.00047$ (strain at which the transition occurs), and $a = 8000$ (steepness of the transition). Note that the range of strains over which the measurements actually take place is about -0.06% to 0.04% , so the model extrapolation outside of that range may not be accurate (for example, based on this data, the value of E_{\max} is not clear, so the four-point bend test data is used as a guide—i.e., the highest modulus observed in that data was 81 GPa). Note that the four-point bending data is actually providing an averaged modulus over the beam thickness, which is experiencing a range of positive and negative strains, which makes it non-trivial to compare those results with the one from the direct modulus measurements. Hence, in this paper we will merely note that the two sets of results are consistent.

Next, given that we have seen such a large (about $2\times$) variation in the modulus as a function of strain, the question arises as to whether other material parameters, like the piezoelectric coefficients, also vary with strain and/or field. For example, other work has reported large increases in d_{31} at high fields for other PZT materials, such as PZT-5A and PZT-5K [20]. Before we describe the measurement setup, we must choose which parameters to measure. Although the Young's modulus (E) and the d_{31} piezoelectric coefficient are the parameters typically used to describe the behavior of a piezoelectric bimorph in actuation mode, d_{31} is not actually an intrinsic material property like the modulus is. That is, when an electric field is applied to a piezoelectric, it is an internal force, or stress, that is produced—the strain that results depends not only on the material properties, but also on the external environment. Hence, in this paper we will refer primarily to a parameter we will call f_{31} , defined as the internal stress produced per unit electric field (i.e. $\frac{\sigma_{1,\text{int}}}{\epsilon_3}$ —this is closely related to the e_{31} piezoelectric coefficient, which is defined as $-\frac{\partial \sigma_1}{\partial \epsilon_3}$ at fixed strain; see the IEEE Standard on Piezoelectricity [21]). This is a more useful parameter in our case, since we are looking at high-field and high-strain effects in which these material properties are not constant, and we would also like to be able to easily apply the results from bulk material measurements to bimorph actuators (described in section 2.5) which experience varying external forces.

The setup described above provides us with two means of measuring f_{31} : the unconstrained contraction of the PZT when electric fields are applied (i.e. with the force sensor disconnected) and the measured forces when the force sensor is connected. The first of these gives d_{31} directly from the raw data (i.e. measured strain divided by applied electric field), but the (compressive) strain increases along with the applied electric field, so these two effects are not separated. Figure 10(d) shows that d_{31} increases rapidly as the field/strain is increased, but then decreases again more gradually. Since we have already determined that E is primarily dependent on the strain, it makes sense to look at the intrinsic material property f_{31} instead, to determine whether any of the variation in d_{31} can be attributed to this source. To this end, for each free contraction measurement made we use figure 10(c) (and/or equation (3)) to find the stress that must be present given the measured strain—this results in the plot

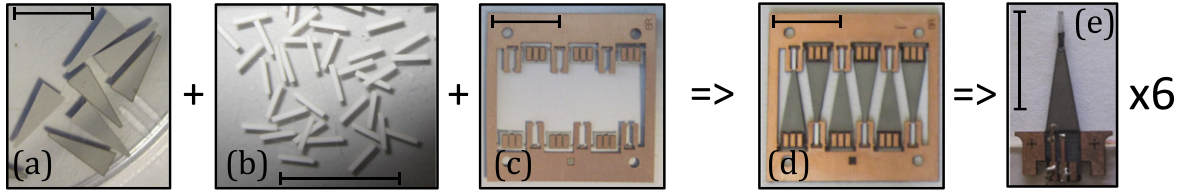


Figure 11. Process steps for ‘standard’ actuator manufacturing. (a) Laser-scored and cleaved PZT. (b) Laser-cut alumina tips. (c) Laser-cut copper-clad FR4; photoresist mask used to wet-etch copper. (d) PZT and alumina manually placed into FR4 jig and bonded to CF using a heat press. (e) Final actuators after release cut with laser, and conductive epoxy applied. Each scale bar is 1 cm long.

shown in figure 10(e). As can be seen, f_{31} does not decrease at high fields/strains like d_{31} does, but rather remains approximately constant after its initial increase. Now that we have removed the effect of the modulus increasing with increasing compressive strain, we can use our measurements from the setup with the force sensor connected to help determine whether the f_{31} variation is due to the field or the strain. First, we can find the stress at zero strain for each applied field (i.e. the blocked force) from the shift in stress that was required to line up the stress–strain plots shown in figure 10(c) (recall that this shift was exactly the stress at zero strain for fields of $1.11 \text{ V } \mu\text{m}^{-1}$ and below, since that condition was encountered for those fields, and this is assumed to be approximately valid for higher fields as well). Dividing by the electric field then gives f_{31} at zero strain, which is also plotted in figure 10(e). As can be seen, the plots of f_{31} at zero strain and at varying strain are not exactly the same, deferring by up to 30%. This indicates that f_{31} does depend on strain as well as field. Note that the value of f_{31} expected from the PZT’s data sheet (which is likely based on low field measurements) is $320 \text{ pm V}^{-1} \times 62 \text{ GPa} \approx 20 \text{ Pa m V}^{-1}$ —our free deflection d_{31} measurements come close to the reported value at low fields and strains (370 pm V^{-1} at $0.22 \text{ V } \mu\text{m}^{-1}$), but our low-strain modulus measurements are a bit lower than the reported value. In addition, our blocked force measurements do not extend to sufficiently low fields to verify that they match with the low-field free deflection measurements, but we assume that f_{31} must approach the same value for both cases at low fields and strains. With this in mind, we have the following picture: f_{31} increases substantially (70–90%) as the electric field is increased from about $0.3\text{--}0.6 \text{ V } \mu\text{m}^{-1}$, and is slightly higher at higher compressive strains. Since we know the strains encountered during the free deflection test, we propose the following simple model—a weak linear dependence of f_{31} on strain combined with a sigmoid function that decreases slightly at higher fields for the field dependence:

$$f_{31} = (1 + b \cdot \epsilon) \times \left(f_{31,\min} + \left(f_{31,\max} (1 - d \cdot \mathcal{E}) - f_{31,\min} \right) \frac{e^{c(\mathcal{E}-\mathcal{E}_0)}}{1 + e^{c(\mathcal{E}-\mathcal{E}_0)}} \right), \quad (5)$$

where $f_{31,\min} = 14 \text{ Pa m V}^{-1}$, $f_{31,\max} = 29 \text{ Pa m V}^{-1}$, $d = 69 \times 10^{-9} \text{ m V}^{-1}$, $\mathcal{E}_0 = 0.4 \text{ V } \mu\text{m}^{-1}$, $c = 10^{-5}$, and $b = -230$ (recall that we have defined compressive strain to be negative). There remains a slight discrepancy between the two sets of data and this model at fields below $0.5 \text{ V } \mu\text{m}^{-1}$, but our operation is almost always well beyond this, and the

measurement precision is also less for smaller deflections, so we will ignore this for the purposes of this paper. Also, note that this model, as well as the model for the modulus variation, is not based on specific physical principles (which is beyond the scope of this paper), but rather meant as a simple fit to the bulk property data that will be used later (section 2.5) to predict actuator behavior. That said, the determination of the physical source of the variations (i.e. strain and/or field) is crucial for predicting actuator behavior, as different strains can be encountered for same field in different situations (e.g. blocked force versus free deflection versus free beam contraction).

2.5. Complete actuator

Now that we have at hand several methods for improving the performance of bulk PZT, we proceed to apply these lessons to bimorph actuator manufacturing to determine their effect on actuator performance. The actuators are fabricated as follows (these steps are illustrated in figure 11): first, individual pieces of PZT (figure 11(a)) and alumina (figure 11(b)) (two of each per actuator) are cut out using the laser (scored and cleaved for the PZT). The alumina is used as a rigid extension affixed to the tip of the actuator—it serves both to amplify the actuator deflection and, along with a trapezoidal shape for the PZT, to distribute stress more uniformly along the length of the actuator when an external load is applied at the actuator’s tip [16]. Copper-clad FR-4 serves as the base material—the copper allows traces to be patterned for electrical contacts, and the FR-4 material is amenable to use in the pin-alignment process (PZT and alumina can not be used easily in pin-alignment, due to their brittle nature). Thus, a jig of copper-clad FR-4 is cut with the laser, and a photoresist mask is used to etch traces in the copper (figure 11(c)). The individual PZT and alumina pieces are then placed carefully into this jig (note: the PZT, alumina, and FR-4 are all cleaned with IPA to promote adhesion), using a slightly tacky layer (gelpak 8) to hold the pieces in place. Two copies are made, and a layer of carbon fiber composite (CF) is sandwiched in between, using pins to align all of the layers. The CF is patterned to match the actuator outlines prescribed by the alignment jig. The CF is used both to adhere the two layers of the bimorph together, and to provide electrical contact to the inner surfaces of the PZT (see diagrams in figures 12(a) and (c)). This sandwich is then placed into a heat press, which serves to cure the resin in the CF—a temperature of $180 \text{ }^\circ\text{C}$ and pressure of about 10 psi for two hours are used to form a good bond to the PZT, alumina, and FR-4 (figure 11(d)). After this, the laser is then

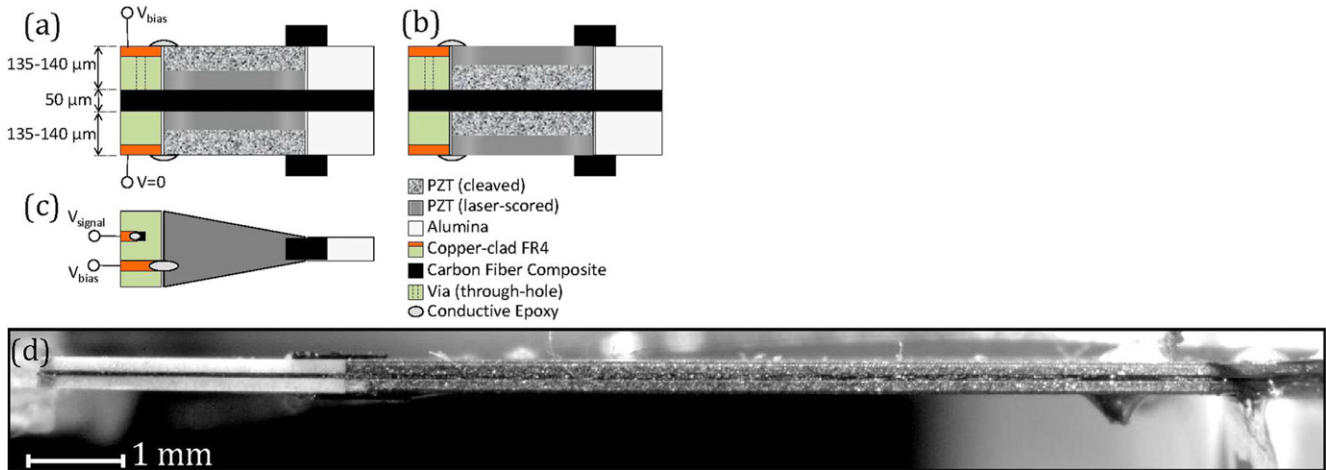


Figure 12. (a) Side-view diagram of the ‘laser-in’ PZT bimorph actuators. (b) Same as (a), but for the ‘laser-out’ actuators. (c) Top-view diagram of the actuators. (d) Side-view photo of one of the actuators positioned for blocked-force measurements.

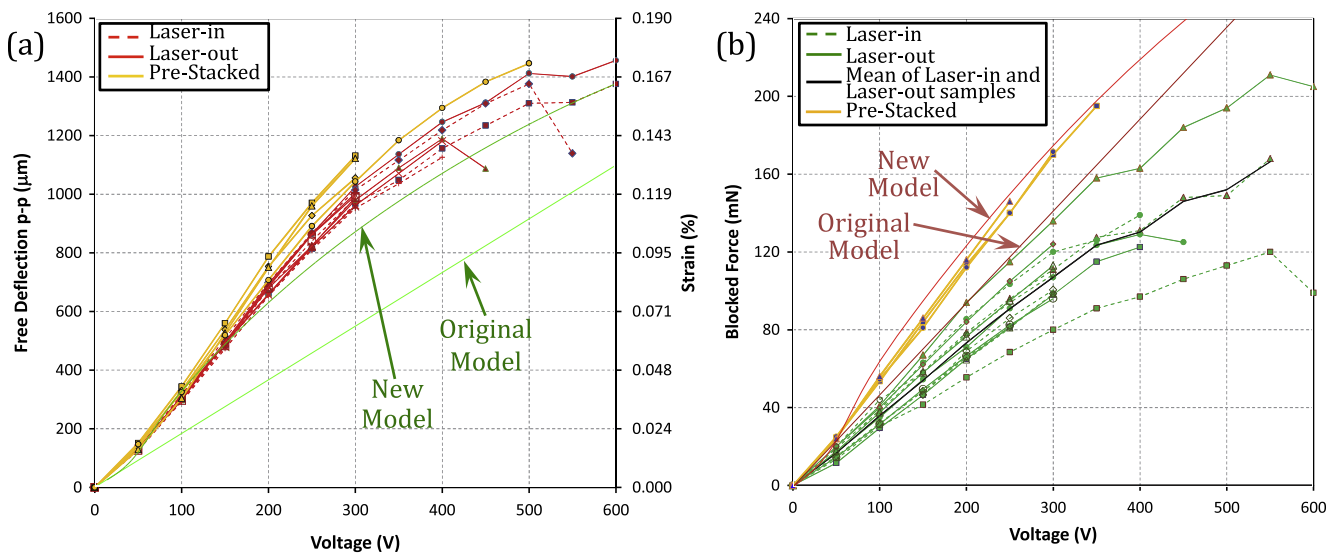


Figure 13. A comparison of ‘laser-in’ and ‘laser-out’ actuators, along with the standard linear model and the new model presented in section 2.5.1. Also shown are results for the ‘pre-stacked’ actuators discussed in section 2.3. (a) Free deflection (peak-to-peak) and maximum surface strain. (b) Blocked force (one-way).

used to cut the individual actuators out of the alignment jig. The final steps are to electrically connect the PZT to the copper traces—this is done using conductive epoxy for each of the three connections (one on each outer PZT surface, and one through a via hole in the FR-4 to the central CF)—and to attach ‘bridges’ at the interface between the PZT and alumina extension. The ‘bridges’ prevent bending at this interface, and are affixed manually with CA glue. An example of a completed actuator is shown in figure 11(e).

2.5.1. Energy density. To measure the effect of laser-induced melting on actuator performance, we fabricate actuators in which the PZT pieces are laser-scored about 50% of the way through the material thickness and then cleaved. One set of actuators is assembled so that the laser-scored edges are on the inner side, while the other set has the laser-scored edges on the outside (figures 12(a) and (b)). These actuators are

characterized through three tests—free deflection and blocked force as a function of applied electric field, and lifetime (covered in section 2.5.2) under loaded conditions close to half of the free deflection, half blocked force operating point (which provides maximum power output for a spring load).

Free deflection is measured optically, viewing the actuator from the side (figure 12(d)), while blocked force is measured by positioning a force sensor (Nano17) so that it just touches the tip of the actuator when the actuator is off (figure 12(d)). In addition, side-view video is also recorded during the force measurements, which is crucial for diagnostic purposes, as we shall see later. Finally, endurance measurements are performed by affixing a spring load to the actuator, positioned so that the deflection under load is close to half of the free deflection—the other end of the spring is affixed to the force sensor, so both force and deflection (from video) are obtained. Figure 13(a) shows the results of the free-deflection

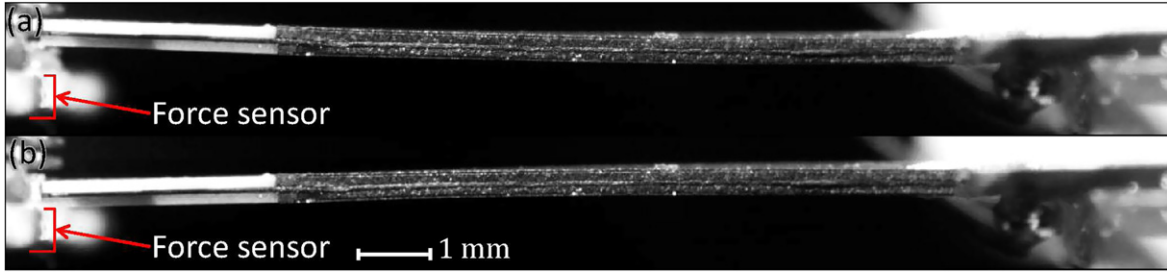


Figure 14. Example of an actuator with a weak base attachment. (a) The actuator in free upward deflection. (b) The same actuator in ‘blocked force’ (note: with no applied field, the actuator’s neutral position is just touching the force sensor).

measurements, with the surface strain also indicated, while figure 13(b) shows the blocked forces. The strain is calculated as $\epsilon = \frac{D\delta}{L^2}$, where D is the total actuator thickness, δ is the deflection (one-way) of the tip of the PZT, and L is the length of the PZT (recall that there is a rigid extension affixed to the end of the PZT, and the peak-to-peak deflection values are for the end of this extension).

Most of the actuators were characterized only up to 300 V, but several were tested by increasing the voltage until failure—most of these failures occurred during blocked force measurements, and shorting was one of the main culprits. Note that only at very high fields ($4.3\text{--}4.4 \text{ V } \mu\text{m}^{-1}$, or 600 V for our case) does the strain on the actuators’ surfaces approach the instantaneous failure strain measured for high fields (figure 10), so we do not necessarily expect to see a clear difference between the ‘laser-in’ and ‘laser-out’ samples in these tests. In particular, figure 10 showed that the failure strain drops to about 0.18% by $3 \text{ V } \mu\text{m}^{-1}$, and is not changing much at those fields (e.g. about 0.19% at $2.2 \text{ V } \mu\text{m}^{-1}$), while the actuators only reach 0.17% strain if they are brought to $4.4 \text{ V } \mu\text{m}^{-1}$ (figure 13(a)), which is the highest we could reach in this setup.

The blocked force measurements (figure 13(b)) show a considerable variation in performance sample-to-sample—for

example of this is shown in figure 14—as can be seen, the curvature in ‘blocked force’ is a substantial fraction (about 75% in this case) of the curvature in free deflection).

As expected, little difference is seen between the ‘laser-in’ and ‘laser-out’ samples, in terms of their energy density at a given electric field, but we will take a moment here to consider what deflections and forces we should expect given the bulk material properties of the PZT.

The standard piezoelectric bimorph equations, including adjustment factors to account for the effect of the rigid extension and trapezoidal shape of the actuator [16] are as follows:

$$\delta_{p-p} = 0.5 \frac{(d_{31}E_P)t_P(t_P + t_{CF})L_{act}^2 \mathcal{E} \left(1 + 2\frac{L_{ext}}{L_{act}}\right)}{\frac{1}{3}E_P t_P (1.5t_{CF}^2 + 3t_{CF}t_P + 2t_P^2) + \frac{E_{CF}t_{CF}^3}{12}} \quad (6)$$

$$F_b = 0.75 \frac{(d_{31}E_P)W_{nom}t_P(t_P + t_{CF})\mathcal{E}}{L_{act}} \text{GF}, \quad (7)$$

where

$$\text{GF} = \frac{8(1 - w_r)^3 \left(1 + 2\frac{L_{ext}}{L_{act}}\right)}{-6(w_r - 1)(-3 + 4l_r(w_r - 1) + 2w_r) + 3(-2 + 2l_r(w_r - 1) + w_r)^2 \ln\left(\frac{2 - w_r}{w_r}\right)}, \quad (8)$$

example, at 300 V the mean force was 107 mN, but with a standard deviation of $\pm 13\%$. Careful inspection of the videos recorded during the blocked force tests reveals that bending is occurring at the interface between the PZT and the base FR4, and the actuators that show a smaller amount of such bending have a higher force output. This indicates that a more rigid attachment mechanism is needed at this interface, just as ‘bridges’ are used at the interface with the extension. In fact, by comparing the curvature of the PZT in free deflection (κ_f) to that in blocked force (κ_b ; which would ideally be zero), we can obtain an estimate of the expected blocked force: $F_{b,\text{exp}} = \frac{F_{b,\text{meas}}}{1 - \kappa_b/\kappa_f} \approx 150\text{--}170 \text{ mN}$ for these actuators. An

where δ_{p-p} is the peak-to-peak deflection at the actuator tip, d_{31} is the piezo coefficient, E_P is the modulus of the PZT, E_{CF} is the modulus of the carbon fiber, t_P is the thickness of the PZT, t_{CF} is the thickness the carbon fiber, L_{act} is the length of the PZT, \mathcal{E} is the applied electric field, L_{ext} is the length of the alumina extension, F_b is the blocked force (one-way), w_{nom} is the average width of the PZT, w_r is the width ratio (the width of the PZT’s base divided by w_{nom}), and l_r is the length ratio $\left(\frac{L_{ext}}{L_{act}}\right)$. Using the values for d_{31} and E_P reported in the PZT’s data sheet (320 pm V and 62 GPa), these equations are plotted in figure 13 along with the measured data. As can be seen, this model predicts deflections only about half of what our

measurements indicate, and the force prediction is 32% higher than the mean of our measurements. Recall that our measurements in section 2.4 showed that f_{31} and E_p actually vary with applied field and strain, providing a possible explanation for the discrepancy we see in our actuator performance. To confirm, we must adjust equations (6) and (7) to account for the actual dependencies of the material properties. Blocked force is simpler—since the strain is ideally very small in this configuration, we approximate the result by plugging in the field dependency of f_{31} (i.e. $d_{31} \times E$) at zero strain (from equation (5)). That is

$$F_{b,\text{new}} \approx 0.75 \times \frac{\left(f_{31,\text{min}} + \left(f_{31,\text{max}}(1 - d \cdot \mathcal{E}) - f_{31,\text{min}} \right) \frac{e^{c(\mathcal{E}-\mathcal{E}_0)}}{1 + e^{c(\mathcal{E}-\mathcal{E}_0)}} \right) W_{\text{nom}} t_P (t_P + t_{CF}) \mathcal{E}}{L_{\text{act}}} \text{GF.} \quad (9)$$

For free deflection, we need to account for both the strain and field dependencies of f_{31} and E_p . Since the strain in the PZT is actually varying through its thickness when the actuator is bent, this would require a relatively complex calculation in which the neutral axis of the actuator actually shifts position depending on how much the actuator is bent (a rough estimate gives a shift of about $10 \mu\text{m}$ when the surface strain is 0.12%). This affects both the stiffness of the beam and the moment arm over which the contraction force in the PZT plate acts, but these two effects partially cancel. Hence, to simplify matters, we will instead use the following approximations: (1) the internal contraction force is approximated as being constant through the thickness of the PZT, with its value determined by the strain at the center of the PZT (and the applied field). That is, we include the dependencies of f_{31} by replacing the $E_p \times d_{31}$ term in the numerator of equation (7) with equation (5)'s f_{31} expression, using the strain in the center of the PZT (which of course depends on the deflection, but this still yields a unique solution). (2) We obtain an effective average modulus of the PZT by finding the modulus at the center of each PZT plate and taking the average. Note that the way these equations are written, we want the secant modulus (i.e. $\frac{\sigma}{\epsilon}$) rather than the local modulus ($\frac{\partial \sigma}{\partial \epsilon}$), so we use equation (3) divided by the strain. (3) Since the strain in the inactive PZT plate (i.e. no field applied) is always positive (i.e. extensive), and the modulus is close to constant in that regime (at least out to 0.04% strain; see figure 10(c)), we can approximate the modulus of the inactive plate as E_{min} independent of strain. Putting all of this together yields the following expression for the free deflection:

where: $E_{P,1} \approx E_{\text{min}}$ (this is the PZT plate which is inactive and in tension),

$$E_{P,2} \approx E_{\text{min}} - \frac{E_{\text{max}} - E_{\text{min}}}{a \cdot \epsilon} \left(\ln(1 + e^{a(\epsilon_0 - \epsilon)}) - \ln(1 + e^{a\epsilon_0}) \right), \quad (11)$$

$$\epsilon = -\delta_{p-p} \frac{t_P + t_{CF}}{2 \left(1 + 2 \frac{L_{\text{ext}}}{L_{\text{act}}} \right) L_{\text{act}}}. \quad (12)$$

Plots generated from these equations are also shown in figure 13—looking first at free deflection, we see that the prediction is now much closer to the data, although the prediction is still up to 15% too low at higher fields. Besides the approximations made above, this may be due to the modulus only having been measured directly between -0.06% and 0.04% strain (figure 10), and extrapolated to include the range of strains encountered (up to $\pm 0.12\%$ surface strain for our typical operation up to 300 V) in the actuator deflection. For blocked force, on the other hand, our prediction is now substantially (63%) higher than the mean observed values, but given the variation in these measurements due to insufficiently rigid base attachments, the model may be indicating what could be achieved in the ideal case. In fact, we will see in section 3 that we can indeed get much closer (within about 5%) to the model's predictions for blocked force.

2.5.2. Endurance. We now move on to endurance tests to see whether the increase in bulk-material failure strain leads to an increase in lifetime when operated with the same deflection at the actuator tip (Note: due to the variation in available force, the position of the load spring is varied slightly to bring the deflections under load close to the same value). Figure 15 shows that the mean lifetime of the 'laser-out' actuators is 5 h (2×10^6 cycles), which is 5 times greater than that of the 'laser-in' actuators. This confirms that the increased failure strain does indeed translate to large improvements in actuator lifetime. Such a large increase in lifetime (5 \times) resulting from a relatively small change in failure strength (about 20%) is not unexpected for a brittle material. For example, from [22] the rate of crack propagation is proportional to $\left(\frac{\sigma}{\sigma_{\text{max}}} \right)^n$, with n of order 1 for ductile materials, but of order 10 for brittle materials. Since $1.2^{10} \approx 6$, this is consistent with our observations.

2.5.3. Other considerations. Another possible effect that could result in a difference between the experimental actuator

$$\delta_{p-p,\text{new}} \approx 0.5 \frac{\left(1 + b \cdot \epsilon \right) \left(f_{31,\text{min}} + \left(f_{31,\text{max}}(1 - d \cdot \mathcal{E}) - f_{31,\text{min}} \right) \frac{e^{c(\mathcal{E}-\mathcal{E}_0)}}{1 + e^{c(\mathcal{E}-\mathcal{E}_0)}} \right) t_P (t_P + t_{CF}) L_{\text{act}}^2 \mathcal{E}}{\frac{1}{3} \frac{E_{P,1} + E_{P,2}}{2} t_P (1.5 t_{CF}^2 + 3 t_{CF} t_P + 2 t_P^2) + \frac{E_{CF} t_{CF}^3}{12}} \left(1 + 2 \frac{L_{\text{ext}}}{L_{\text{act}}} \right), \quad (10)$$

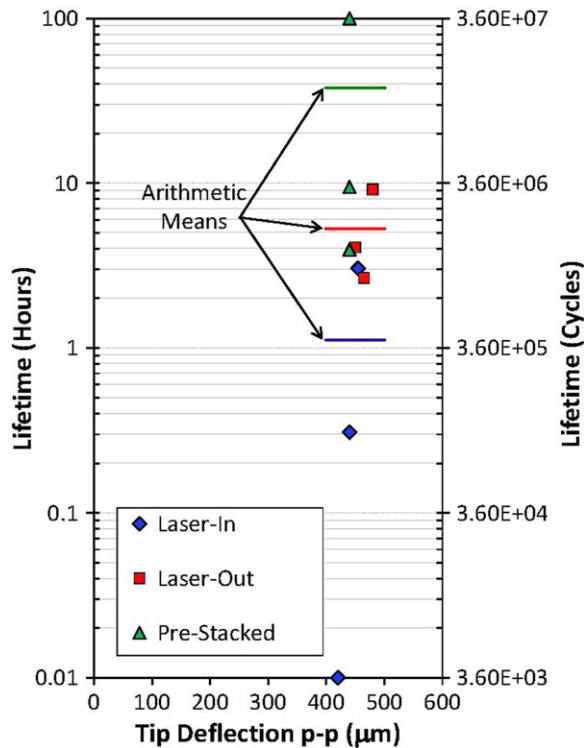


Figure 15. Endurance comparison for ‘laser-in’ actuators versus ‘laser-out’ actuators. Also shown are results for the ‘pre-stacked’ actuators discussed in section 3. All tests are performed at 100 Hz.

behavior and the model is aspect ratio (i.e. $\frac{W_{nom}}{L_{act}}$). For example, too large an aspect ratio could lead to bending along the width as well as the length of the actuator, and too small an aspect ratio could result in changed performance if the laser affects d_{31} in some region around the laser cuts. To verify that we not in a regime where these effects are significant, we fabricate actuators with aspect ratio twice that used as our standard in this paper (2/9), as well as some with half the aspect ratio, and compare their results. Figure 16(a) shows that the free deflection of these three aspect ratios is nearly identical, and figure 16(b) shows that the blocked forces per unit width of the actuator are also very close (note that for the smaller aspect ratio actuators, the tip width is only 250 μm , which led to partial failure of the tip bridges, and is likely the cause of the reduced forces (about 10% lower) at higher fields). Therefore, we may safely conclude that neither of the proposed aspect ratio effects is significant for the actuators tested in this paper.

3. Maximizing ease of fabrication—eliminating the need for manual assembly

In this section, we describe a ‘pre-stacked’ method of actuator manufacturing that removes many of the manual steps in the previous process (as well as rendering those that remain less important), improves energy density by 70% and reduces force output variability through the use of rigid attachments, and further increases mean lifetime by a factor of >6, for a

total increase of >30 \times as compared to the original actuators. In this approach, strips of material are first bonded together into a ‘stack’, followed by laser rastering of via holes and copper traces and laser cutting on both sides of the stack to separate the actuators. In this way, the only manual steps are the alignment of the initial strips of material (which is less crucial, as the release cuts form a precisely defined shape regardless of this alignment) and application of conductive epoxy to the central CF layer.

3.1. Fabrication

In more detail, the first step is to cut rectangles of PZT, alumina, and CF (figures 17(a), (b))—the length of the PZT rectangle fixes the length of the PZT in each actuator, but the width of each actuator can be chosen later as desired. The length of the alumina sets an upper bound for the extension length in the final actuators. Simple FR-4 jigs (figure 17(c)) are used to align the two sets of PZT and alumina rectangles (note: the PZT, alumina, and FR-4 are all cleaned with IPA to promote adhesion), which are then bonded with a central CF layer in a heat press to form the initial ‘pre-stack’ (figure 17(d)). An additional set of CF layers is then cut which will ‘bridge’ the PZT-alumina interface, along with a similar copper layer. The CF provides a strong mechanical attachment between the PZT and both the extension and the base alumina, as well as electrical contact to the outer PZT surfaces. The copper allows for easy soldering to the electrical contacts. These CF and copper layers are then pin-aligned with the existing ‘pre-stack’ and cured again in the heat press (recall that the CF contains epoxy resin which forms a strong bond on curing) (figure 17(e)). The resulting ‘pre-stack’ can now be treated as an individual sheet of composite material from which nearly arbitrary planar actuators can be cut (restricted only by the length of the PZT part of the actuator). This is enabled by the use of finely tuned laser cutting and etching parameters that allow selective patterning of different layers. These steps must also be performed in a particular order—primarily to ensure that PZT is exposed only to the desired laser powers. The first step is to raster the outer copper and CF layers to form the electrical contact traces. There are a few considerations to keep in mind for this step: (1) we would like to avoid rastering too far into the alumina. (2) The main reason for performing this step first is to avoid having to cut through the copper when cutting the alumina (as this could leave residual copper traces on the edges of the actuator, leading to possible shorting issues); therefore we must take care to raster the copper wherever we plan to cut the alumina. (3) The rastering must avoid the PZT as it is done at high power and could result in shorting of the PZT. Consideration (1) is achieved by tuning the cut settings to the minimum needed to remove the copper and CF (and the alumina is more resistant to cutting than the copper and CF); also in this case some etching into the alumina is not detrimental. Considerations (2) and (3) are achieved by having the copper not extend over the PZT during the ‘pre-stack’ fabrication (the CF provides the electrical connection to the PZT). The second step is to cut through the alumina to define the base and

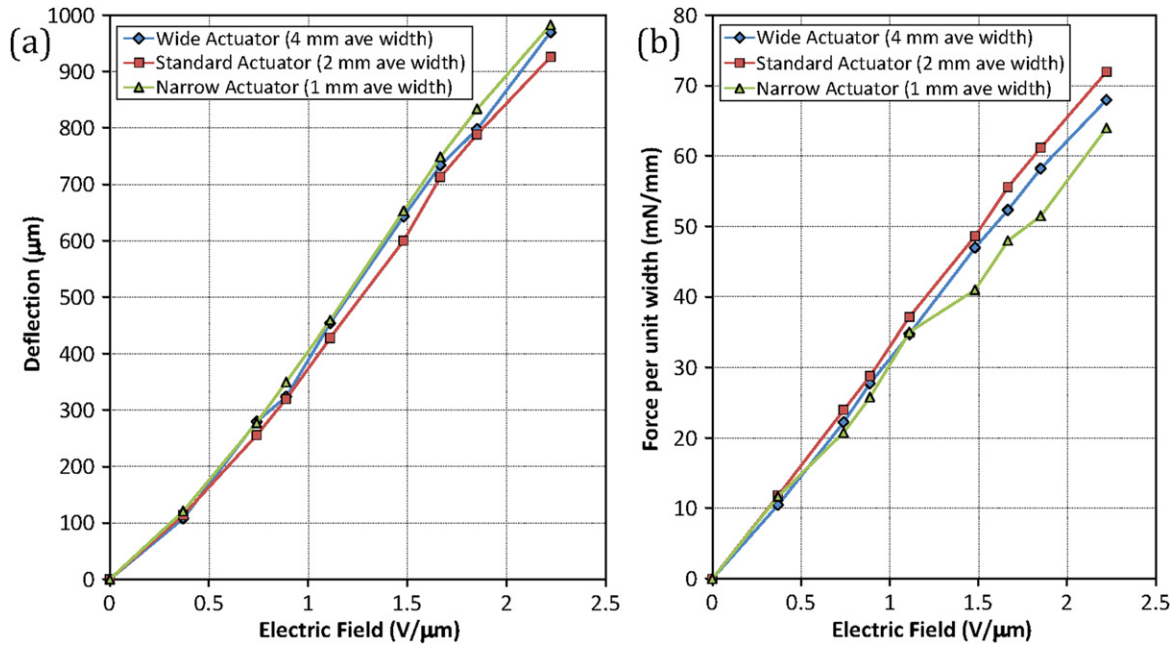


Figure 16. (a) Peak-to-peak free deflection and (b) blocked force (one-way) divided by average width of actuator, for three aspect ratios. These actuators were fabricated using the pre-stacked method described in section 3, but with sub-optimal base bridges.

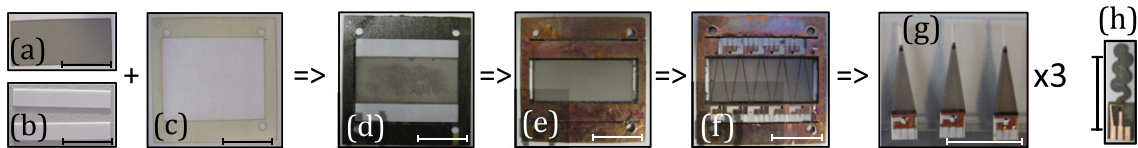


Figure 17. Process steps for ‘pre-stacked’ actuator fabrication process. (a) Laser-scored and cleaved PZT. (b) Laser-cut alumina. (c) Laser-cut FR4. (d) PZT and alumina manually placed into FR4 jig and bonded to CF using a heat press. (e) Additional CF and copper layers are pin-aligned and bonded in heat press. (f) Cut actuators and raster copper using laser. (g) Final actuators after release and conductive epoxy. (h) A serpentine-shaped actuator fabricated to demonstrate the ability to create complicated planar geometries. Each scale bar is 1 cm long.

extension outlines. Due to the difficulty of cutting alumina with the laser, this step is performed at full power to minimize cutting times. In addition, the cut only extends through the alumina on one side of the stack (which will be flipped over later). To fully release the actuators, the alumina cuts must extend to the alumina-PZT boundary, but this could cause shorting of the PZT if there is even the slightest misalignment in the ‘pre-stack’. Therefore, this step must be performed before cutting the PZT to allow the opportunity to remove any damage that may have been caused. This leads us to the third step—through-cutting of the PZT at low power (as with the alumina, this cut also goes through only the PZT on one side of the stack). In addition to defining the actuator shape, this cut is also used to remove any damage to the PZT caused by the high-power alumina cut (by extending it around the end of the alumina cuts). Fourth, we perform the high-power edge-treatment of the PZT, which is offset from the low-power cuts by $10\ \mu\text{m}$, as discussed in section 2.3. Fifth, via holes must be formed through the alumina to make contact with the central CF layer—this is a bit tricky, as the CF can be ablated much more easily than the alumina. However, by etching most of the way through the alumina at full power, and the rest of the

way at low power (in this case achieved by increasing the pulse frequency), the desired selectivity can be achieved. In addition, an alignment mark is cut all the way through the stack, which is then flipped over and steps 1–4 above are repeated for the other side of the stack (via holes to the central CF are only needed on one side). Since the alignment mark is cut through the stack after it is assembled, alignment of the cuts in the top and bottom layers is guaranteed even if slight misalignment in the stacked materials was present (provided that the sample is kept small enough that asymmetrical distortions in the laser system do not become an issue—2 cm samples work well in our system, and larger samples could be handled by splitting the cutting pattern into several sections). Figure 17(f) shows the sample at this stage in the process. The actuators are then separated, cleaned carefully with IPA (especially the edges of the PZT to remove any debris from the laser cuts), and conductive epoxy is applied to the via-holes to make electrical contact to the central CF layer. Since the CF ‘bridges’ provide electrical contact to the outer PZT surfaces, no other conductive epoxy is needed. Finally, the actuators are coated with parylene to prevent electrical breakdown. Several completed actuators are shown in

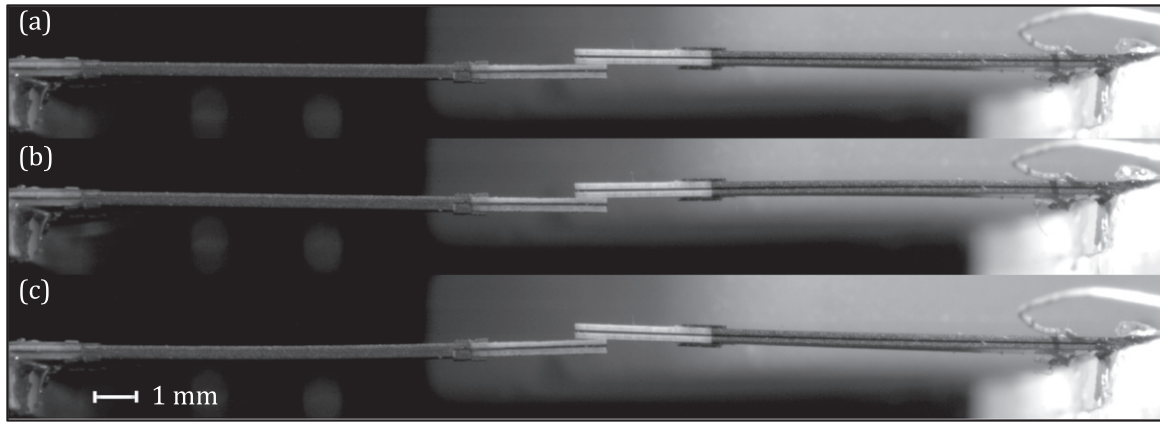


Figure 18. A ‘pre-stacked’ actuator (left) versus a standard actuator (right). (a) Both actuators unpowered. (b) The ‘pre-stacked’ actuator is off, while the standard actuator is commanded to bend downward. (c) The ‘pre-stacked’ actuator is commanded to bend upward, while the standard actuator is off.

figure 17(g). To illustrate the flexibility of this process for actuator design, figure 17(h) shows a ‘serpentine’ shaped actuator that was produced by the same method; only a change in the PZT cut pattern was required. Although this process has more steps than the standard process, nearly all of them require simply inputting the appropriate settings into the laser system—even the generation of the cut patterns to achieve the required offsets, etc, has been mostly automated so that only the dimensions of an individual actuator and the number of actuators is needed.

3.2. Results

We now characterize the actuators fabricated using the ‘pre-stacked’ method described in section 3.1 and compare the results to those obtained for the ‘laser-in’ and ‘laser-out’ actuators described in section 2.5. Figure 13 shows the free-deflection (figure 13(a)) and blocked-force (figure 13(b)) measurements. A slight increase (about 10%) is seen in the free deflection, but the major improvement is in the blocked force—we measure a 58% increase above the mean of the ‘laser-in’ and ‘laser-out’ actuators, as well as a greatly reduced variance. Along with the deflection increase, this results in a 70% increase in energy density at the same electric field. These improvements can be attributed primarily to the addition of the rigid ‘bridges’ at the base of the actuators. In addition, the blocked force performance of these actuators now lines up very closely (within ~5%) with the predictions of the model presented in section 2.5.1 (equation (9)). To demonstrate visually this improvement, one of the ‘pre-stacked’ actuators and one of the standard actuators are positioned such that their tips press against each other when powered. As can be seen from the images in figure 18 (and video in supplemental info), the ‘pre-stacked’ actuator easily wins—in this example, when the standard actuator is powered, it deflects the ‘pre-stacked’ one by $120\ \mu\text{m}$ (figure 18(b)) as compared to the neutral position (figure 18(a)); on the other hand, when the ‘pre-stacked’ actuator is powered, the deflection is $200\ \mu\text{m}$ (figure 18(c)), which is about 70% greater. Finally, we measure the

endurance of the ‘pre-stacked’ actuators—figure 15 shows a comparison of these results to those obtained for the ‘laser-in’ and ‘laser-out’ actuators (on a log scale for ease of viewing). The results show that the mean lifetime has increased by 6–8 \times as compared with the ‘laser-out’ actuators and is 30–40 \times greater than the original ‘laser-in’ actuators (‘laser-in’ mean: 1 h, ‘laser-out’ mean: 5 h, ‘pre-stacked’ mean: 30–40 h). Note that one of the ‘pre-stacked’ actuators has yet to fail at the time of submission of this work, and is currently at 110 h (40×10^6 cycles) of operation. While the failure strain results (section 2.3) for the low-power/high-power combined cut (which is what is used in the ‘pre-stacked’ process) were slightly higher than those of the ‘laser-out’ samples, the main contributor to the increase in lifetime for the ‘pre-stacked’ actuators is likely the base bridges. This is because the base bridges actually substantially reduce the strain experienced (by around 35%) by the PZT for a given tip deflection, and the lower strain translates to a longer lifetime. This can be seen by noting that when there are no base bridges, bending can occur at the base-PZT interface, so if the actuator is trying to push downward, for example, it will actually bend up at the base interface, leading to a greater curvature in the PZT (as in figure 14). It is also worth noting that although the variance in lifetime results is a bit high, the improvements made still show up clearly despite the small sample size. Further, visual inspection of images of the ‘pre-stacked’ actuators indicates a possible explanation for some of the samples failing sooner—for those that failed sooner, the high-power laser treatment zone was narrower in some regions, and it was in these locations that the failures occurred. The extremely long-lasting actuator, on the other hand, had a nearly uniform high-power melt zone. While too few samples were tested to verify this conclusively, it is suggestive of the possibility that all of the actuators could be made to last even longer if the high-power laser treatment can be made more uniform (one possible cause for the non-uniformity is motion of the sample during the cutting process, but further work is required to determine this).

4. Conclusions

This work describes several methods for increasing the energy density and lifetime of piezoelectric bimorph actuators, as well as providing an explanation for the much higher performance of these actuators as compared with the predictions of standard linear models. The take-away lessons are as follows: (1) reducing the roughness of the exposed edges of PZT bimorph actuators results in higher fracture strength, provided that the roughness reduction occurs at the relevant size-scale for crack formation (e.g. the grain size for inter-granular fracture). This can be achieved through multiple methods, such as mechanical polishing and laser-induced melting. Laser-induced melting has the advantage of being more automated, but it reduces the dielectric strength of PZT along with increasing its fracture strength. This effect can be mitigated through carefully combined low power and high power cuts which result in melting only in the regions where it is most needed. The resulting 20% fracture strength improvement led to a 5× increase in mean device lifetime for the same tip deflection. (2) Rigid attachments are crucial, not only between the piezoelectric material and the actuator extension, but also with the actuator base. This prevents bending at this interface, and resulted in a >55% increase in mean blocked force, as well as a much reduced variance (<±2% as compared to ±13% for the standard actuators). This has the additional benefit of reducing the strain in the actuator (for the same tip deflection), resulting in a further increase of >6× in mean lifetime. (3) A new ‘pre-stacked’ fabrication process for piezoelectric actuators was presented as a means to eliminate most manual steps, simplify integration of mechanical bridges and electrical connections, and allow for nearly arbitrary planar actuator designs to be fabricated from the same laminate. (4) The modulus and piezoelectric coefficients of PZT vary substantially with strain and electric field, and these effects must be taken into account to predict actuator behavior above about $0.3 \text{ V } \mu\text{m}^{-1}$. In particular, measurements of these parameters for bulk PZT beams were used to create a model of the PZT behavior; when applied to the conditions present in bimorph actuators, the results were within 5% for blocked force, and 20% for free deflection (even outside the range of strains under which the material properties were measured).

In conclusion, the optimized PZT actuators described in this work output a peak-to-peak free displacement of $1100 \mu\text{m}$ and a peak-to-peak blocked force of 340 mN (when operating at fields of $0\text{--}2.2 \text{ V } \mu\text{m}^{-1}$ and a frequency of 1 Hz), and weigh 42 mg, resulting in an energy density of 4.5 J kg^{-1} (defined as $0.5F_{b,p-p} \times \delta_{f,p-p}$ for performance comparison purposes, as in [16]). For operation at the same fields, this is an increase of about 70% as compared with the mean performance of the standard actuators (and those described in [16]). It is also 2.4 times higher than what the standard linear models would predict. Commercially available bimorphs typically have energy densities around 30 times lower than our results (for example, PiezoSystems’ actuators [23] have a maximum energy density of 0.15 J kg^{-1})—this is primarily due to the higher maximum fields that we can use ($0\text{--}2.2 \text{ V } \mu\text{m}^{-1}$ as

opposed to $\pm 0.3 \text{ V } \mu\text{m}^{-1}$). Due to the different drive technique (as in [16], the actuators are wired such that each plate always experiences a positive field), we do not have a direct comparison at the same field, but our data and models indicate that we would expect about 30% higher performance for our actuators at equivalent fields. Further, the mean lifetime of our actuators (at conditions close to half free deflection and half blocked force) have been increased by more than 30 times, from 1 h (3.6×10^5 cycles) to >30 h ($>10^7$ cycles).

Acknowledgments

The authors gratefully acknowledge support from the National Science Foundation (award # CCF 0926148) and the Wyss Institute for Biologically Inspired Engineering at Harvard. Any opinions, findings, and conclusions or recommendations expressed in this material are those of the authors and do not necessarily reflect the views of the National Science Foundation. In addition, we would like to thank James Weaver for analyzing the chemical composition of our samples.

References

- [1] Ma K Y, Chirarattananon P, Fuller S B and Wood R J 2013 Controlled flight of a biologically inspired, insect-scale robot *Science* **340** 603–7
- [2] Hoffman K L and Wood R J 2010 Towards a multi-segment ambulatory microrobot *IEEE Int. Conf. on Robotics and Automation* pp 1196–1202
- [3] Baisch A T and Wood R J 2009 Design and fabrication of the Harvard ambulatory micro-robot *14th Int. Symp. on Robotics Research* pp 715–30
- [4] Song Y S and Sitti M 2007 Surface-tension-driven biologically inspired water strider robots: theory and experiments *IEEE Trans. Robot.* **23** 578–89
- [5] Sun L, Zhang Y, Sun P and Gong Z 2001 Study on robots with PZT actuator for small pipe *Int. Symp. on Micromechanics and Human Science* pp 149–54
- [6] Tuncdemir S, Ural S O and Uchino K 2009 Meso-scale piezoelectric gripper with high dexterity *Japan. J. Appl. Phys.* **48** 044501-1–044501-8
- [7] Roberts D C, Li H, Steyn J L, Yaglioglu O, Spearing S M, Schmidt M A and Hagood N W 2003 A piezoelectric microvalve for compact high-frequency, high-differential pressure hydraulic micropumping systems *J. Microelectromech. Syst.* **12** 81–92
- [8] Rodrigues G, Bastais R, Roose S, Stockman Y, Gebhardt S, Schoenecker A, Villon P and Preumont A 2009 Modular bimorph mirrors for adaptive optics *Opt. Eng.* **48** 034001
- [9] Mista K 1995 Warp knitting machine with piezoelectrically controlled jacquard patterning *Patent* US5390512 A
- [10] Smithmaitrie P 2009 Analysis and Design of Piezoelectric Braille Display *Rehabilitation Engineering* ed T Y Kheng (Rijeka: InTech) (www.intechopen.com/books/rehabilitation-engineering/analysis-and-design-of-piezoelectric-braille-display)
- [11] Anton S R, Erturk A and Inman D 2012 Bending strength of piezoelectric ceramics and single crystals for multifunctional load-bearing applications *IEEE Trans. Ultrason. Ferroelectr. Freq. Control* **59** 1085–92
- [12] Misri I, Hareesh P, Yang S and DeVoe D L 2012 Microfabrication of bulk PZT transducers by dry film

- photolithography and micro powder blasting *J. Micromech. Microeng.* **22** 085017
- [13] Annoni M, Arleo F, Trolli A, Suarez A and Alberdi A 2012 Fine abrasive water jet machining of piezoelectric ceramics: cutting parameters optimization *21st Int. Conf. Water Jetting*
- [14] Zeng D W, Li K, Yung K C, Chan H L W, Choy C L and Xie C S 2004 UV laser micromachining of piezoelectric ceramic using a pulsed Nd:YAG laser *Appl. Phys. A* **78** 415–21
- [15] Desbiens J-P and Masson P 2007 ArF excimer laser micromachining of Pyrex, SiC and PZT for rapid prototyping of MEMS components *Sensors Actuators A* **136** 554–63
- [16] Wood R J, Steltz E and Fearing R S 2005 Optimal energy density piezoelectric bending actuators *Sensors Actuators A* **119** 476–88
- [17] Hareesh P, Misri I, Yang S and DeVoe D L 2012 Transverse interdigitated electrode actuation of homogeneous bulk PZT *J. Microelectromech. Syst.* **21** 1513–8
- [18] Guillon O, Thiebaud F, Perreux D, Courtois C, Champagne P and Crampon J 2005 New considerations about the fracture mode of PZT ceramics *J. Eur. Ceram. Soc.* **25** 2421–4
- [19] Fushimi S and Ikeda T 1967 Phase equilibrium in the system PbO-TiO₂-ZrO₂ *J. Am. Ceram. Soc.* **50** 129–32
- [20] Morgan Technical Ceramics *Piezoelectric Ceramics Properties and Applications* chapter 5 (www.morganelectroceramics.com/resources/guide-to-piezoelectric-dielectric-ceramic)
- [21] *IEEE Standard on Piezoelectricity* ANSI/IEEE Std 176-1987 (1988) (New York: Institute of Electrical and Electronics Engineers)
- [22] Ritchie R O 1999 Mechanisms of Fatigue-Crack propagation in ductile and brittle solids *Int. J. Fract.* **100** 55–83
- [23] Piezo Systems, Inc. 2014 *Piezo Systems: High Performance Piezoelectric Bending Transducers and Actuators* (<http://piezo.com/prodbm2highperf.html>)